Geophysical Journal International

Geophys. J. Int. (2016) **206,** 825–834
Advance Access publication 2016 March 23
GJI Marine geosciences and applied geophysics

doi: 10.1093/gji/ggw110

Long-range correlations of microseism-band pressure fluctuations in the ocean

Justin S. Ball,[1,2] Oleg A. Godin,[1,3] Läslo G. Evers[4,5] and Cheng Lv[6]

[1]*Cooperative Institute for Research in Environmental Sciences, University of Colorado Boulder,* 216 *UCB, Boulder, CO* 80309, *USA. E-mail: justin.ball@colorado.edu*
[2]*Department of Geological Sciences, University of Colorado Boulder,* 399 *UCB, Boulder, CO* 80309, *USA*
[3]*National Oceanic and Atmospheric Administration/Earth System Research Laboratory,* 325 *Broadway, Boulder, CO* 80305, *USA*
[4]*Department of Seismology and Acoustics, Royal Netherlands Meteorological Institute, PO Box* 201, *NL*-3730 *AE De Bilt, The Netherlands*
[5]*Department of Geoscience and Engineering, Faculty of Civil Engineering and Geosciences, Delft University of Technology, Stevinweg* 1/*PO-box* 5048, 2628 *CN Delft*/2600 *GA Delft, The Netherlands*
[6]*Department of Atmospheric and Oceanic Sciences, University of Colorado Boulder,* 311 *UCB, Boulder, CO* 80309, *USA*

Accepted 2016 March 21. Received 2016 March 18; in original form 2015 November 4

SUMMARY

We investigate the spatial coherence of underwater ambient noise using a yearlong time-series measured off Ascension Island. Qualitative agreement with observed cross-correlations is achieved using a simple range-dependent model, constrained by earlier, active tomographic studies in the area. In particular, the model correctly predicts the existence of two weakly dispersive normal modes in the microseism frequency range, with the group speed of one of the normal modes being smaller than the sound speed in water. The agreement justifies our interpretation of the peaks of the measured cross-correlation function of ambient noise as modal arrivals, with dispersion that is sensitive to crustal velocity structure. Our observations are consistent with Scholte to Moho head wave coupled propagation, with double mode conversion occurring due to the bathymetric variations between receivers. We thus demonstrate the feasibility of interrogating crustal properties using noise interferometry of moored hydrophone data at ranges in excess of 120 km.

Key words: Interferometry; Interface waves; Theoretical seismology; Wave propagation; Acoustic properties; Oceanic hotspots and intraplate volcanism.

1 INTRODUCTION

Wavefields generated by spatially distributed random sources are known to remain partially coherent at points separated by distances that are large compared to the wavelength, with the two-point cross-correlation function of the random wavefields approximating the Green's function, which describes deterministic wave propagation between the two observation points (Lobkis & Weaver 2001; Snieder 2004; Roux *et al.* 2004; Wapenaar 2004; Godin 2006; Gouédard *et al.* 2008). Cross-correlation functions of pressure fluctuations in the ocean have been investigated in the 0.5–30 mHz band, where the correlations characterize deep-water infragravity waves and their sources (Webb 1986; Godin *et al.* 2014b), and at acoustic frequencies above 1 Hz, where geoacoustic parameters of the seafloor (Brown *et al.* 2014), spatial (Godin *et al.* 2010) and temporal (Woolfe *et al.* 2015) variations of the sound speed in water and ocean current velocity (Godin *et al.* 2014a) have been retrieved from noise cross-correlations.

Here, we study one of the most energetic parts of the ambient noise spectrum, the microseism band between 0.1 and 1 Hz, and investigate what information about the ocean and the seafloor can be retrieved from the cross-correlations of pressure fluctuations. This effort is motivated, in part, by successful applications of wave interferometry to the microseism-band seismic noise recorded by seismometers located on land (Sabra *et al.* 2005; Shapiro *et al.* 2005; Gerstoft *et al.* 2006; Bensen *et al.* 2007; Brooks *et al.* 2009) and on the seafloor (Harmon *et al.* 2007; Yao *et al.* 2011; Takeo *et al.* 2014; Tian *et al.* 2013; Zha *et al.* 2014). Using methodology developed by the seismic community for extracting fundamental and higher mode Rayleigh wave arrivals (Yao *et al.* 2011) from ambient noise, we obtain robust dispersion measurements from long-range correlations in the microseism band for the first time using moored hydrophone data.

This study is based on a yearlong time-series of underwater ambient noise measured during 2011 off Ascension Island in the Central Atlantic. The Comprehensive Nuclear-Test-Ban Treaty Organization (CTBTO) maintains a global network of hydrophones for the passive monitoring of global nuclear testing as part of the International Monitoring System (IMS). In addition to their primary mission, IMS hydrophone data have been previously used to characterize the ocean and ambient noise coherence at acoustic frequencies (Sabra *et al.* 2013; Evers *et al.* 2014; Evers & Snellen 2015;

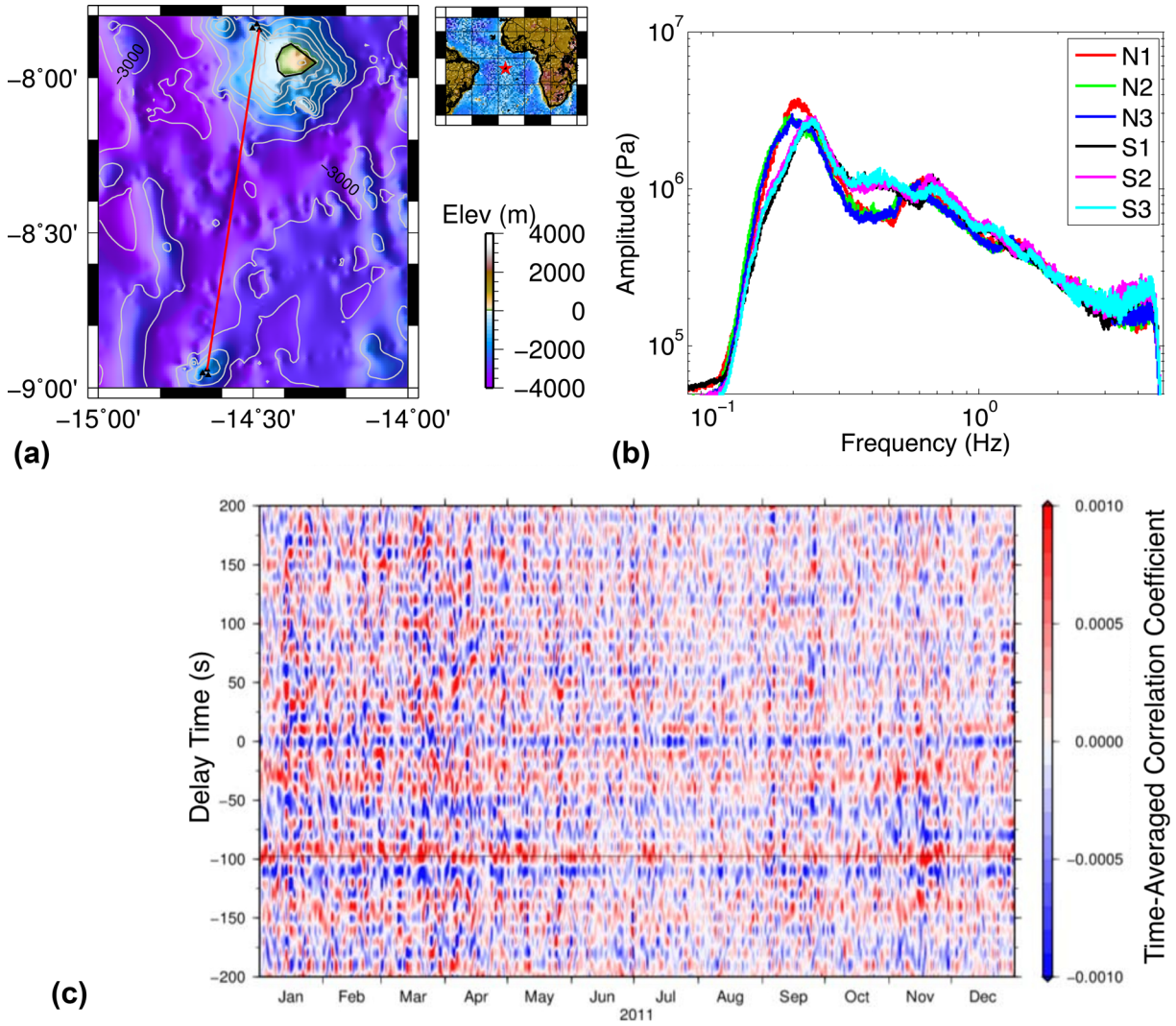

Figure 1. (a) Ascension Island CTBTO arrays with red line connecting elements N1 and S1. S1 element coordinates are 8.9412S, 14.480W, and N1 is located at 7.8457S, 14.480W. (b) Noise power spectra from 2011 January and (c) daily cross-correlation functions between stations N1 and S1 over year 2011, showing seasonal variation in amplitudes.

Woolfe *et al.* 2015). The hydrophone station at Ascension consists of two triangular arrays spaced 123 km apart along a line oriented roughly NE-SW (Fig. 1a). The array element spacing is 2 km, and the hydrophones are moored within the Sound Fixing And Ranging (SOFAR) channel at about 850 m depth, where data are continuously recorded at a sample frequency of 250 sps. Noise spectra from all Ascension elements show a prominent secondary microseism peak centred at 5 s period (Fig. 1b), and southern elements (S1–S3) exhibit higher amplitudes than their northern counterparts (N1–N3) in shorter periods of the microseism band, from 2 to 3.3 s.

2 NOISE CORRELATION IN THE MICROSEISM BAND

To estimate Green's functions from the noise data, we follow closely the method of Yao *et al.* (2011). Data are windowed into tapered 60 min segments, demeaned and detrended. Spectral whitening is applied before one-bit normalization, to suppress the influence of energetic transient signals. The pre-processed windows are then bandpass filtered in four period ranges (1–4, 3–6, 5–8 s and 7–11 s) and cross-correlated in the time domain. The resulting cross-correlation functions are filtered again in the same bands to mitigate the non-linear effects of one-bit normalization before they are averaged to yield the estimated daily and yearly interarray Green's functions.

Our correlation functions exhibit prominent temporal variation in amplitudes over year 2011 (Fig. 1c), with the greatest signal energy generally occurring during the Northern Hemisphere winter from January to March. These variations are consistent with the expected mechanisms of secondary microseism noise generation by non-linear wave interaction in the north Atlantic, where a strong source region has been identified to the south of Greenland (Stehly *et al.* 2006; Kedar *et al.* 2008; Tian & Ritzwoller 2015). Despite these amplitude variations, the arrival times of the dominant peaks remain stationary in time. Once the approximate Green's functions have been determined, we use frequency–time analysis (FTAN; Dziewonski & Hales 1972; Bensen *et al.* 2007) to estimate group velocity dispersion from the spectrogram of the yearly average cross-correlation function (Fig. 2).

We observe two primary modes that are weakly dispersive but have very distinct group speeds. Of these two dominant arrivals, one propagates at a group speed of $\sim$1 km s^{-1}, slower than the

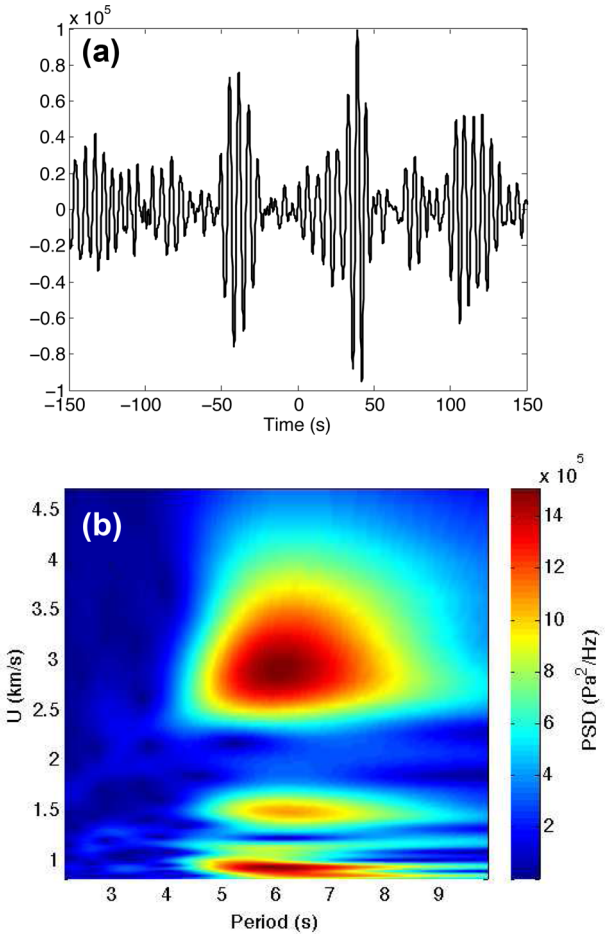

Figure 2. (a) Yearly average cross-correlation function for station path N1–S1, filtered in the microseism band (2–10 s). (b) Spectrogram showing period-dependent group velocity (U) and power spectral density (PSD) of symmeterized cross-correlation function. FTAN measurements presented in Fig. 4 were obtained from the separate positive and negative lag spectrograms (not shown).

$\sim$1.5 km s^{-1} average speed of sound in water and the other mode propagates faster than the speed of sound in water at $\sim$3 km s^{-1}. Additionally, we observe what appears to be a lower energy signal with a group speed of 1.5 km s^{-1} that is close to the average sound speed in the water column and does not exhibit strong dispersion (Fig. 2b).

The difference between the dispersion curves retrieved from positive and negative time delays (Fig. 2b) provides an estimate of accuracy of our dispersion curve retrieval from the noise cross-correlations. Our forward and reverse measurements differ by $\sim$100 m s^{-1} for the fundamental mode and $\sim$80 m s^{-1} for the first overtone.

3 RANGE-DEPENDENT DISPERSION MODELLING

Bathymetry, and therefore the propagation conditions for seismoacoustic waves, vary strongly along the propagation path (Fig. 3a). This is made evident by the strong variation in higher mode cut-off periods along the N1–S1 path (Fig. 3b) and by comparison of dispersion curves that are modeled for various ocean depths between the stations (Figs 3b and c).

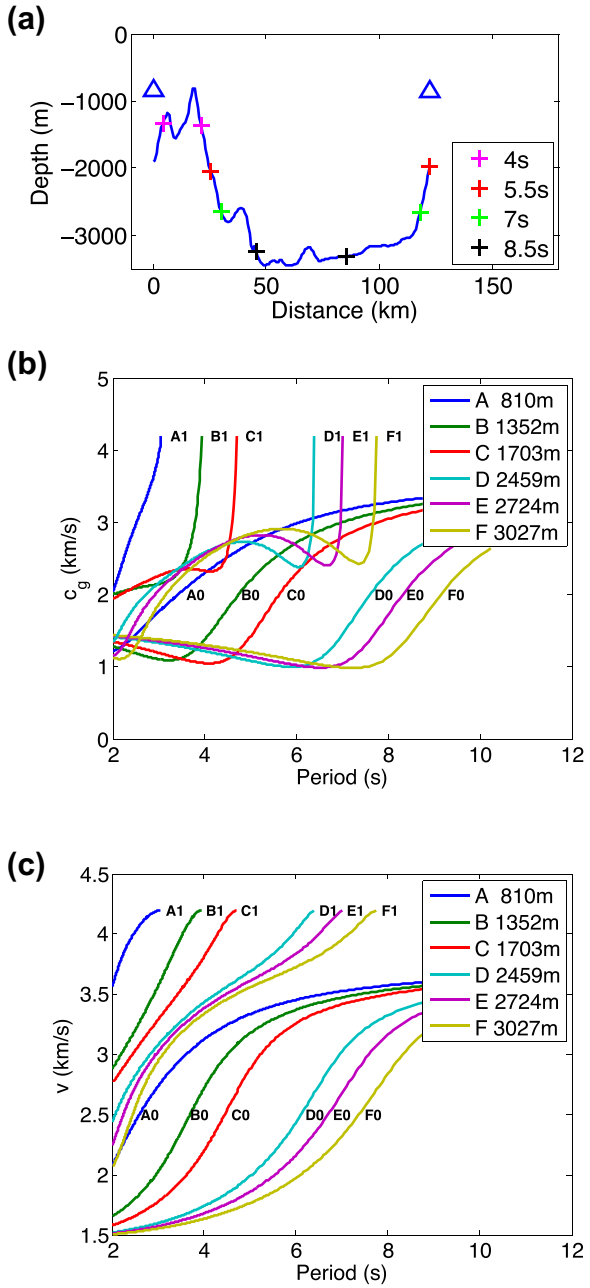

Figure 3. (a) Bathymetric profile between stations N1 and S1 (triangles), with crosses showing locations of mode 1 cut-offs at 4, 5.5, 7 and 8.5 s. (b) Group dispersion curves for first two modes computed using a subset of locations along the N1–S1 path. Curves are labeled with the water depth of each model and the mode number (0 or 1). Note the variation in mode 1 cut-off period with water depth. (c) Phase dispersion curves corresponding to the models shown in (b).

To model seismoacoustic wave propagation, we employ the adiabatic approximation (Brekhovskikh & Godin 1999) and disregard horizontal refraction. In this approximation, the modal phase and traveltime in the horizontally inhomogeneous waveguide are obtained, respectively, by integration of the accumulated phase and traveltime from a series of 1-D dispersion curves modeled using the bathymetric variations along the N1–S1 station path (see Appendix A).

Our bathymetric model is a hybrid of satellite altimetry (Smith & Sandwell 1997) and multibeam sonar data where available. The

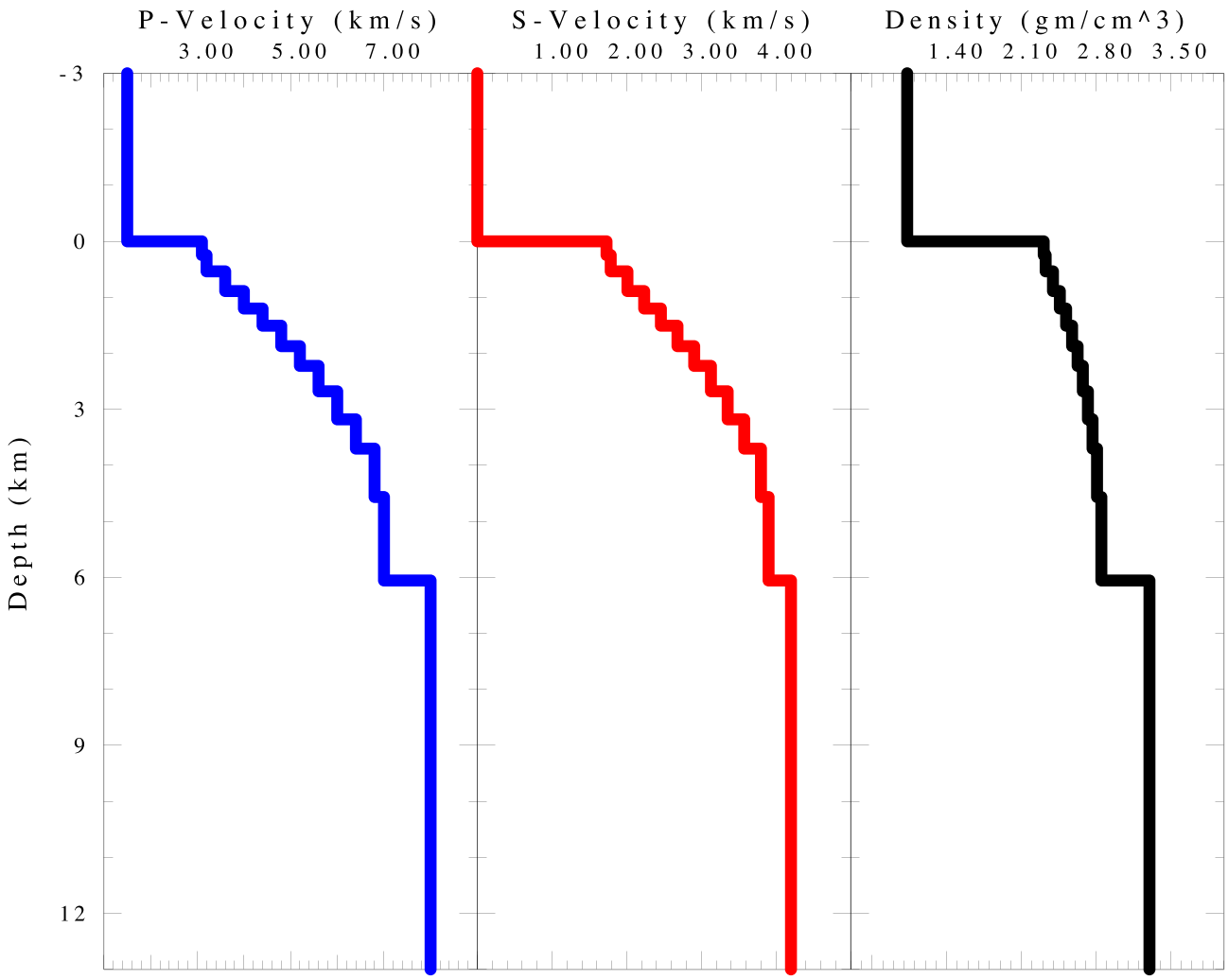

Figure 4. Representative *P*-velocity (v_p), *S*-velocity (v_s) and density models for a single node on the N1–S1 path. Our *P*-velocity model is adapted from the tomography results of Evangelidis *et al.* (2004).

latter was provided by CTBTO. Water depths increase over the first 50 km to the southwest of N1 from 1 to ∼3 km, then generally remain constant for much of the central portion over the abyssal plain, until decreasing again to ∼2 km on the flank of the seamount to which the southern hydrophones are moored.

We use a compressional velocity (v_p) model for the flank of Ascension Island based on the *P*-wave tomography of Evangelidis *et al.* (2004). In this model, v_p increases from 3 km s^{-1} at the seafloor to greater than 8 km s^{-1} at 10 km depth (typical of oceanic upper mantle). Shear velocities (v_s) in the crust were estimated from the v_p model using a v_p/v_s ratio of 1.78, which we chose based on trial values within the range $v_p/v_s = 1.74 \pm 0.09$ reported by Mocquet *et al.* (1989) for Atlantic oceanic crust younger than 50 Ma. We then estimate density from v_p using the empirical relation of Carlson & Raskin (1984). Beneath the ocean and crustal layers is a half-space with shear velocity of 4.2 km s^{-1} and compressional velocity of 8.0 km s^{-1}, based on the Moho speed from Evangelidis *et al.* (2004). The solid Earth properties are assumed to have the same dependence on the depth below seafloor at every point along the propagation path. Fig. 4 shows model v_p, v_s and density profiles for one water depth (3 km) along the N1–S1 path. We show group velocity sensitivity kernels computed for this model in Fig. 5. Our sensitivity kernels illustrate that mode 1 is generally sensitive to deeper structure than mode 0, and both modes' sensitivity to v_s extends to greater depths than their sensitivity to v_p.

We calculate dispersion at 176 nodes along the interarray path using the CPS330 software package of Herrmann & Ammon (2004). The software yields fundamental and higher mode group and phase velocity dispersion curves at each node, in a period range spanning 2–10 s. The resulting suite of dispersion curves was then path-integrated at each period to produce a dispersion curve for the entire propagation path between stations N1 and S1. In calculating dispersion curves in the range-dependent waveguide, the phase and group speeds of the first mode are formally set to equal the shear velocity in the half-space when the cut-off frequency of the mode is higher than the wave frequency. The physical meaning of this assumption is discussed below. Our modelling results are shown in Fig. 6. While we did not perform an inversion in this study, the path-integrated dispersion we obtain generally agrees with our observations. Various terms have historically been used to describe guided waves that propagate within a model of a fluid layer over an elastic half-space, including 'Stoneley waves' (Ewing *et al.* 1957), 'pseudo-Rayleigh waves' (Scholte 1949; Roever *et al.* 1959), 'Rayleigh waves' (Harmon *et al.* 2007), 'Rayleigh–Scholte waves' (Yao *et al.* 2011) and 'Scholte waves' (Cagniard 1962; Bromirski *et al.* 2013). In the

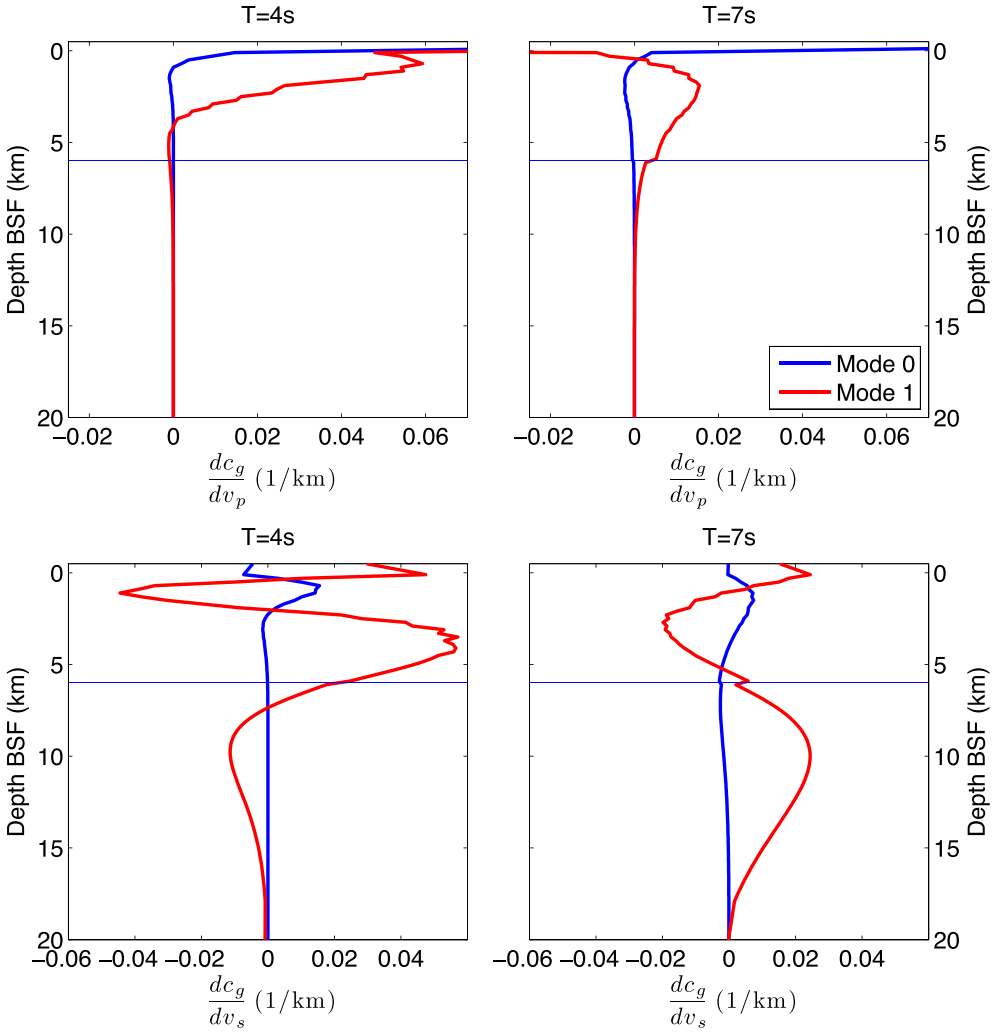

Figure 5. Group velocity sensitivity kernels computed for the models shown in Fig. 4, at periods of 4 and 7 s. Partial derivatives of group velocity c_g with respect to shear velocity v_s and compressional velocity v_p are shown as a function of depth below seafloor (BSF). The Moho is represented by the blue reference line at 6 km BSF.

strict sense, Scholte waves are surface waves that exist at the plane interface between homogeneous fluid and solid half-spaces (Roever *et al.* 1959; Cagniard 1962; Brekhovskikh & Godin 1998). Here, we follow (Essen *et al.* 1998; Park *et al.* 2005; Kugler *et al.* 2007; Vanneste *et al.* 2011; Soloway *et al.* 2015) and use the term 'Scholte waves' more broadly to designate those normal modes in the fluid–solid waveguide which are strongly affected by fluid parameters and the shear rigidity of the ocean bottom.

We interpret the slower arrival (to which we refer as mode 0) as the fundamental mode of Scholte waves (Cagniard 1962). Unlike Scholte waves in an ocean with a constant depth, our modelling predicts weak dispersion on the N1–S1 path, in agreement with the observations (Figs 2b and 6). To understand this result, note that, in the 2-D adiabatic approximation, the effective group slowness of a normal mode is a path average of the local (i.e. calculated for a given, constant ocean depth) group slownesses. In our environmental model, only ocean depth changes along the propagation path, and the path average is a (weighted) average over ocean depths. Averaging over depth is similar to averaging over frequency (as illustrated by a dispersion equation for a simplified problem in Appendix B), which suppresses the strong dispersion of local normal modes.

At shortest periods, the faster arrival can be interpreted as first Scholte wave overtone (mode 1). However, in most of the frequency band we analyse, mode 1 encounters a cut-off at one or more (typically two) points along the N1–S1 path (Fig. 3a). We therefore interpret this fast arrival as a converted, or hybrid, wave, which propagates as a refracted, vertically polarized shear wave along the Moho on those parts of the N1–S1 path where the first mode is cut-off. In our environmental model we have a fluid layer, which overlays a stratified solid layer on a homogeneous solid half-space. At cut-off, the phase and group speeds of a normal mode equal the shear wave speed in the half-space, and theory (Brekhovskikh & Godin 1999) predicts that the bulk of the normal energy continues propagating past the cut-off in the same direction (as opposed to being reflected) as the head wave with the shear wave speed.

4 DISCUSSION AND CONCLUSIONS

Results of modelling the frequency-dependent traveltimes for the hybrid wave are in agreement with observations (Fig. 6). Typically, we have doubly converted waves. The theory of coupling between the discrete (normal modes) and continuous (body waves) spectra of

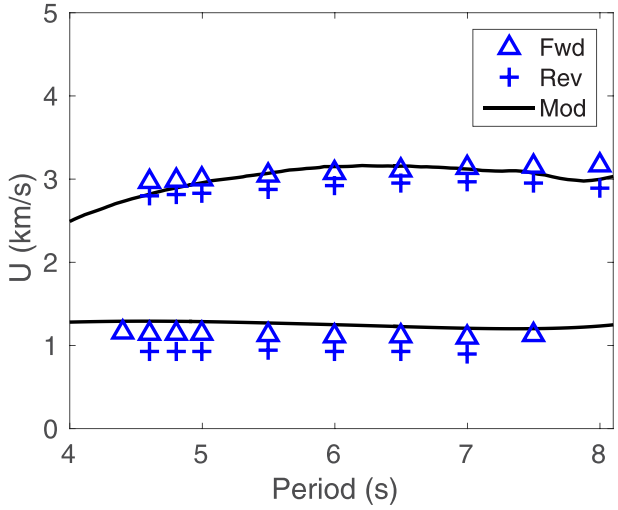

Figure 6. Measured dispersion of the cross-correlation function of stations N1–S1 (symbols), shown with prediction from path-integrating 1-D dispersion curves computed for a range-dependent model based on the results of Evangelidis *et al.* (2004) (solid lines).

the wavefield is reviewed in Brekhovskikh & Godin (1999), including double conversion in the case of an acoustic (fluid) waveguide. To our knowledge, this is the first observation of doubly converted seismoacoustic waves in the ocean. As seen in Fig. 6, the first overtone data are fit well with our simple range-dependent propagation model, while the fundamental mode is fit more poorly, with our model exhibiting a systematic offset of $+200$ m s^{-1} from the observations. This may indicate either a higher sensitivity of the fundamental mode to cross-range environmental gradients, the effects of which we have neglected, or a need to refine the v_p and v_s models used in our calculations.

The sensitivity of the converted wave's traveltime to shear speed in the upper mantle is of practical significance. Because of the rich frequency content of ambient noise, noise interferometry can serve as a powerful tool to reveal new propagation regimes in 2-D and 3-D inhomogeneous ocean.

We have shown that noise interferometry in the microseism band is practical using data from hydrophones tethered ∼1 km above the seafloor, at interarray distances exceeding 120 km. We interpret the two major peaks in the Green's functions to be Scholte modes, exhibiting dispersion that is sensitive to the 2-D acoustic–elastic properties of the ocean and underlying crust along the propagation path. We find that path-integrated dispersion from a model incorporating prior tomographic results and the along-track bathymetry agrees generally with our observations. Our modelling indicates that the fundamental mode exhibits strong dependence on the v_p and thickness of the water layer, while the higher mode is sensitive to velocity structure at greater relative depths in the crust and upper mantle (Fig. 5).

Observed power spectra of pressure fluctuations in the water column have a pronounced peak in the microseism frequency band. Long (∼1 km or longer) wavelengths of seismoacoustic waves in this band make evaluation of the noise cross-correlations insensitive to tidally induced motions of IMS moorings, which are expected to result in horizontal displacements of hydrophones in the tens of metres. The results presented here, which we obtained using hydrophones on long moorings, indicate that hydrophone-equipped autonomous underwater vehicles and floats can provide useful data for interferometric studies of the seafloor in the microseism frequency band. We have demonstrated the feasibility of inverting the dispersion of Ascension hydrophone correlations for uppermost-mantle shear velocities. Our results imply that crustal structure can be investigated using passive data from hydrophones instead of ocean bottom seismometers, assuming the hydrophones are deployed where similar coupling conditions to those at Ascension exist. Ascension Island's tectonic origin remains in debate. The volcanic edifice is presumed to be either the surface expression of a hotspot, or the result of melt produced by the interaction of the Ascension fracture zone to the north with the nearby Mid-Atlantic Ridge to the east (Gaherty & Dunn 2007). It is conceivable that future work on the data investigated here can contribute to discerning between competing models of Ascension's genesis, and a greater overall understanding of ridge–hotspot interaction processes.

ACKNOWLEDGEMENTS

We thank the CTBTO and station operators for the high quality of the IMS data and products, and M.K. Prior and M. Zampolli of CTBTO for their input on technical issues. We also thank S.C. Webb for his helpful insights. The hydroacoustic data used in this study are available from the virtual Data Exploitation Center (vDEC) at http://ctbto.org/specials/vdec. This work was supported, in part, by the National Science Foundation, grant OCE1129524, and NAVAIR, award N68335-12-C-0104. L.E.'s contribution was partly funded through a VIDI project from the Dutch Science Foundation (NWO), project number 864.14.005.

REFERENCES

Bensen, G., Ritzwoller, M., Barmin, M., Levshin, A., Lin, F., Moschetti, M., Shapiro, N. & Yang, Y., 2007. Processing seismic ambient noise data to obtain reliable broad-band surface wave dispersion measurements, *Geophys. J. Int.,* **169,** 1239–1260.

Brekhovskikh, L.M. & Godin, O.A., 1998. *Acoustics of Layered Media. 1: Plane and Quasi-Plane Waves,* 2nd edn, pp. 87–112, Springer-Verlag.

Brekhovskikh, L.M. & Godin, O.A., 1999. *Acoustics of Layered Media. 2: Point Sources and Bounded Beams,* 2nd edn, pp. 243–320, Springer-Verlag.

Bromirski, P.D., Stephen, R.A. & Gerstoft, P., 2013. Are deep-ocean-generated surface-wave microseisms observed on land?, *J. geophys. Res.,* **118,** 1–20.

Brooks, L.A., Townend, J., Gerstoft, P., Bannister, S. & Carter, L., 2009. Fundamental and higher-mode Rayleigh wave characteristics of ambient seismic noise in New Zealand, *Geophys. Res. Lett.,* **36,** L23303, doi:10.1029/2009GL040434.

Brown, M.G., Godin, O.A., Williams, N.J., Zabotin, N.A., Zabotina, L. & Banker, G.J., 2014. Acoustic Green's function extraction from ambient noise in a coastal ocean environment, *Geophys. Res. Lett.,* **41,** 5555–5562.

Cagniard, L., 1962. *Reflection and Refraction of Progressive Seismic Waves,* pp. 244–246, McGraw-Hill.

Carlson, R.L. & Raskin, G.S., 1984. Density of the ocean crust, *Nature,* **311,** 555–558.

Dziewonski, A. & Hales, A., 1972. Numerical analysis of dispersed seismic waves, *Methods Comput. Phys.,* **11,** 39–85.

Essen, H.H., Grevemeyer, I., Herber, R. & Weigel, W., 1998. Shear-wave velocity in marine sediments on young oceanic crust: constraints from dispersion analysis of Scholte waves, *Geophys. J. Int.,* **132**(1), 227–234.

Evangelidis, C.P., Minshull, T.A. & Henstock, T.J., 2004. Three-dimensional crustal structure of Ascension Island from active source seismic tomography, *Geophys. J. Int.,* **159,** 311–325.

Evers, L.G. & Snellen, M., 2015. Passive probing of the sound fixing and ranging channel with hydro-acoustic observations from ridge earthquakes, *J. acoust. Soc. Am.,* **137,** 2124–2136.

Evers, L.G., Brown, D., Heaney, K.D., Assink, J.D., Smets, P.S.M. & Snellen, M., 2014. Evanescent wave coupling in a geophysical system: airborne acoustic signals from the M_w 8.1 Macquarie Ridge earthquake, *Geophys. Res. Lett.,* **41,** 1644–1650.

Ewing, W.M., Jardetzky, W.S. & Press, F., 1957. *Elastic Waves in Layered Media,* pp. 162–164, McGraw-Hill Book Company, Inc.

Gaherty, J.B. & Dunn, R.A., 2007. Evaluating hot spot–ridge interaction in the Atlantic from regional-scale seismic observations, *Geochem. Geophys. Geosyst.,* **8,** Q05006, doi:10.1029/2006GC001533.

Gerstoft, P., Sabra, K.G., Roux, P., Kuperman, W.A. & Fehler, M.C., 2006. Green's functions extraction and surface-wave tomography from microseisms in southern California, *Geophysics,* **71**(4), SI23–SI31.

Godin, O.A., 2002. A 2-D description of sound propagation in a horizontally inhomogeneous ocean, *J. Comput. Acoust.,* **10,** 123–151.

Godin, O.A., 2006. Recovering the acoustic Green's function from ambient noise cross-correlation in an inhomogeneous moving medium, *Phys. Rev. Lett.,* **97,** 054301, doi:10.1103/PhysRevLett.97.054301.

Godin, O.A., Zabotin, N.A. & Goncharov, V.V., 2010. Ocean tomography with acoustic daylight, *Geophys. Res. Lett.,* **37,** L13605, doi:10.1029/2010GL043623.

Godin, O.A., Brown, M.G., Zabotin, N.A., Zabotina, L. & Williams, N.J., 2014a. Passive acoustic measurement of flow velocity in the Straits of Florida, *Geosci. Lett.,* **1,** doi:10.1186/s40562-014-0016-6.

Godin, O.A., Zabotin, N.A., Sheehan, A.F. & Collins, J.A., 2014b. Interferometry of infragravity waves off New Zealand, *J. geophys. Res.,* **118,** 1103–1122.

Gouédard, P. *et al.*, 2008. Cross-correlation of random fields: mathematical approach and applications, *Geophys. Prospect.,* **56,** 375–393.

Harmon, N., Forsyth, D. & Webb, S., 2007. Using ambient seismic noise to determine short-period phase velocities and shallow shear velocities in the young oceanic lithosphere, *Bull. seism. Soc. Am.,* **97,** 2009–2023.

Herrmann, R.B. & Ammon, C.J., 2004. Surface waves, receiver functions and crustal structure, in *Computer Programs in Seismology,* Version 3.30, St. Louis Univ., Saint Louis, MO.

Kedar, S., Longuet-Higgins, M., Webb, F., Graham, N., Clayton, R. & Jones, C., 2008. The origin of deep ocean microseisms in the North Atlantic Ocean, *Proc. R. Soc. A,* **464,** 777–793.

Kugler, S., Bohlen, T., Forbriger, T., Bussat, S. & Klein, G., 2007. Scholte-wave tomography for shallow-water marine sediments, *Geophys. J. Int.,* **168**(2), 551–570.

Lobkis, O.I. & Weaver, R.L., 2001. On the emergence of the Green's function in the correlations of a diffuse field, *J. acoust. Soc. Am.,* **110,** 3011–3017.

Mocquet, A., Romanowicz, B. & Montagner, J.P., 1989. Three-dimensional structure of the upper mantle beneath the Atlantic Ocean inferred from long-period Rayleigh waves: 1. Group and phase velocity distributions, *J. geophys. Res.,* **94**(B6), 7449–7468.

Mordret, A., Shapiro, N.M., Singh, S., Roux, P., Montagner, J.-P. & Barkved, O.I., 2013. Azimuthal anisotropy at Valhall: the Helmholtz equation approach, *Geophys. Res. Lett.,* **40,** 2636–2641.

Park, C.B., Miller, R.D., Xia, J., Ivanov, J., Sonnichsen, G.V., Hunter, J.A. & Christian, H., 2005. Underwater MASW to evaluate stiffness of water-bottom sediments, *Leading Edge,* **24**(7), 724–728.

Press, F., Ewing, M. & Tolstoy, I., 1950. The Airy phase of shallow-focus submarine earthquakes, *Bull. seism. Soc. Am.,* **40,** 111–148.

Roever, W.L., Vining, T.F. & Strick, E., 1959. Propagation of elastic wave motion from an impulsive source along a fluid/solid interface, *Phil. Trans. R. Soc. Lond., A,* **251,** 455–523.

Roux, P., Kuperman, W.A. & the NPAL Group, 2004. Extracting coherent wave fronts from acoustic ambient noise in the ocean, *J. acoust. Soc. Am.,* **116,** 1995–2003.

Sabra, K.G., Gerstoft, P., Roux, P., Kuperman, W.A. & Fehler, M.C., 2005. Extracting time-domain Green's function estimates from ambient seismic noise, *Geophys. Res. Lett.,* **32,** L03310, doi:10.1029/2004GL021862.

Sabra, K.G., Fried, S., Kuperman, W.A. & Prior, M., 2013. On the coherent components of low-frequency ambient noise in the Indian Ocean, *J. acoust. Soc. Am.,* **133,** EL20–EL25.

Scholte, J.G., 1949. On true and pseudo Rayleigh waves, *Proceedings Koninklijke Nederlandse Akademie van Wetenschappen,* **52,** 652–653.

Shapiro, N.M., Campillo, M.L. & Ritzwoller, M.H., 2005. High-resolution surface-wave tomography from ambient seismic noise, *Science,* **307,** 1615–1618.

Smith, W.H.F. & Sandwell, D.T., 1997. Global seafloor topography from satellite altimetry and ship depth soundings, *Science,* **277,** 1957–1962.

Snieder, R., 2004. Extracting the Green's function from the correlation of coda waves: a derivation based on stationary phase, *Phys. Rev. E,* **69,** 046610, doi:10.1103/PhysRevE.69.046610.

Soloway, A.G., Dahl, P.H. & Odom, R.I., 2015. Modeling explosion generated Scholte waves in sandy sediments with power law dependent shear wave speed, *J. acoust. Soc. Am.,* **138**(4), EL370–EL374.

Stehly, L., Campillo, M. & Shapiro, N.M., 2006. A study of the seismic noise from its long-range correlation properties, *J. geophys. Res.,* **111**(B10), 1978–2012.

Takeo, A., Forsyth, D.W., Weeraratne, D.S. & Nishida, K., 2014. Estimation of azimuthal anisotropy in the NW Pacific from seismic ambient noise in seafloor records, *Geophys. J. Int.* **199**(1), 11–22.

Tian, Y. & Ritzwoller, M.H., 2015. Directionality of ambient noise on the Juan de Fuca plate: implications for source locations of the primary and secondary microseisms, *Geophys. J. Int.,* **201**(1), 429–443.

Tian, Y., Shen, W. & Ritzwoller, M.H., 2013. Crustal and uppermost mantle shear velocity structure adjacent to the Juan de Fuca Ridge from ambient seismic noise, *Geochem. Geophys. Geosyst.,* **14,** 3221–3233.

Vanneste, M. *et al.*, 2011. On the use of the Norwegian Geotechnical Institute's prototype seabed-coupled shear wave vibrator for shallow soil characterization – I. Acquisition and processing of multimodal surface waves, *Geophys. J. Int.,* **185**(1), 221–236.

Wapenaar, K., 2004. Retrieving the elastodynamic Green's function of an arbitrary inhomogeneous medium by cross correlation, *Phys. Rev. Lett.,* **93,** 254301, doi:10.1103/PhysRevLett.93.254301.

Webb, S.C., 1986. Coherent pressure fluctuations observed at two sites on the deep sea floor, *Geophys. Res. Lett.,* **13,** 141–144.

Weinberg, H. & Burridge, R., 1974. Horizontal ray theory for ocean acoustics, *J. acoust. Soc. Am.,* **55,** 63–79.

Woolfe, K.F., Lani, S., Sabra, K.G. & Kuperman, W.A., 2015. Monitoring deep-ocean temperatures using acoustic ambient noise, *Geophys. Res. Lett.,* **42,** 2878–2884.

Yao, H., Gouédard, P., Collins, J.A., McGuire, J.J. & van der Hilst, R.A., 2011. Structure of young East Pacific Rise lithosphere from ambient noise correlation analysis of fundamental-and higher-mode Scholte–Rayleigh waves, *C. R. Geosci.,* **343,** 571–583.

Zha, Y., Webb, S.C., Wei, S.S., Wiens, D.A., Blackman, D.K., Menke, W., Dunn, R.A. & Conder, J.A., 2014. Seismological imaging of ridge–arc interaction beneath the Eastern Lau Spreading Center from OBS ambient noise tomography, *Earth planet. Sci. Lett.,* **408,** 194–206.

APPENDIX A: GUIDED PROPAGATION OF SEISMOACOUSTIC WAVES IN A HORIZONTALLY INHOMOGENEOUS OCEAN

Consider linear seismoacoustic waves in an ocean where physical parameters, including the ocean depth, vary gradually in the horizontal plane. The spatial scale of the horizontal variations is assumed to be large compared to the wavelength. The ocean is stationary in the absence of waves. Let seismoacoustic waves be generated by a monochromatic point source of mass with the amplitude a_0 of the volume injection

rate. Within the water column, acoustic pressure p (i.e. wave-induced perturbation in the pressure at a given point) satisfies the reduced wave equation (Brekhovskikh & Godin 1999)

$$\nabla \cdot \left(\frac{\nabla p}{\rho} \right) + \frac{\omega^2 p}{\rho c^2} = i\omega a_0 \delta(\boldsymbol{R} - \boldsymbol{R}_1) \tag{A1}$$

where ω is the wave frequency, ρ and c are the water density and sound speed, $\delta(\cdot)$ is the Dirac delta function, $\boldsymbol{R} = (x, y, z)$ and $\boldsymbol{R}_1 = (x_1, y_1, z_1)$ is the location of the wave source.

In a horizontally invariant waveguide, the seismoacoustic wavefield can be represented as a superposition of normal modes, which propagate horizontally without coupling. Generally, horizontal inhomogeneities in a waveguide lead to energy exchange (coupling) between the modes. In the case of gradual, slow variation of the waveguide parameters with horizontal coordinates, wave propagation can be asymptotically described in the adiabatic approximation (Weinberg & Burridge 1974; Brekhovskikh & Godin 1999), where each mode adjusts to the varying propagation conditions without coupling to the other normal modes. Conditions of validity of the adiabatic approximation are discussed, for example, in Brekhovskikh & Godin (1999). These conditions are typically met in the ocean in the frequency range considered in the main text. In the adiabatic approximation, the acoustic pressure in a normal mode excited in a horizontally inhomogeneous waveguide by the point source in eq. (A1) is (Weinberg & Burridge 1974; Brekhovskikh & Godin 1999)

$$p(\boldsymbol{R}, \omega) = i\omega a_0 P(z; \boldsymbol{r}) P(z_1; \boldsymbol{r}_1) G(\boldsymbol{r}, \boldsymbol{r}_1) \tag{A2}$$

where $\boldsymbol{r} = (x, y)$ and $\boldsymbol{r_1} = (x_1, y_1)$ are 2-D horizontal vectors and the function G satisfies the 2-D Helmholtz equation

$$\partial^2 G(\boldsymbol{r}, \boldsymbol{r}_1)/\partial \boldsymbol{r}^2 + k^2(\boldsymbol{r}) G(\boldsymbol{r}, \boldsymbol{r}_1) = \delta(\boldsymbol{r} - \boldsymbol{r}_1) \tag{A3}$$

with radiation conditions at $|\boldsymbol{r} - \boldsymbol{r_1}| \to \infty$. Here, $P(z; \boldsymbol{r})$ and $k(\boldsymbol{r})$ are the mode shape function (i.e. the vertical profile of pressure) and the mode wavenumber in an auxiliary, horizontally homogeneous waveguide having the same depth, seabed properties and sound speed and density profiles that the original, horizontally inhomogeneous waveguide has at the given x and y.

The function G can be viewed as the Green's function of the 2-D Helmholtz equation (eq. A3), that is, the field due to a unit point source in the 2-D problem in the horizontal plane. It satisfies the reciprocity relation $G(\boldsymbol{R}, \boldsymbol{R_1}) = G(\boldsymbol{R_1}, \boldsymbol{R})$. An asymptotic solution for $G(\boldsymbol{R}, \boldsymbol{R_1})$ can be found in the ray, or geometric optics, approximation (Weinberg & Burridge 1974; Brekhovskikh & Godin 1999). In this approximation, normal modes propagate from the wave source along horizontal trajectories (rays). The position of a point $\boldsymbol{r}(l, \phi)$ on a horizontal ray and the mode wave vector $\boldsymbol{k}(l, \phi) = (k_x, k_y)$ at this point are found from the differential ray equations

$$d\boldsymbol{r}/dl = \boldsymbol{k}/k, \quad d\boldsymbol{k}/dl = \partial k/\partial \boldsymbol{r}, \tag{A4}$$

where l and ϕ are the arc length along the ray and the azimuthal angle giving the direction of the ray at the source. For a generic dependence of the ocean depth on horizontal coordinates, eqs (A4) have to be integrated numerically. In the ray approximation,

$$G(\boldsymbol{r}, \boldsymbol{r}_1) = \left[8\pi \left(k_x \left(\frac{\partial y}{\partial \varphi} \right)_l - k_y \left(\frac{\partial x}{\partial \varphi} \right)_l \right) \right]^{-1/2} \exp\left(i\Phi(\boldsymbol{r}, \boldsymbol{r}_1) - \frac{3i\pi}{4} \right), \quad \Phi(\boldsymbol{r}, \boldsymbol{r}_1) = \int_{r_1}^{r} k dl. \tag{A5}$$

Integration in eq. (A5) is along an eigenray, that is, the horizontal ray that connects points r_1 and r. In a horizontally homogeneous ocean, $\partial k/\partial \boldsymbol{r} = 0$, horizontal rays are straight lines, $x = x_1 + l\cos\varphi$, $y = y_1 + l\sin\varphi$ and eq. (A5) simplifies to $G(\boldsymbol{r}, \boldsymbol{r_1}) = (8\pi k|\boldsymbol{r} - \boldsymbol{r_1}|)^{-1/2} \exp(ik|\boldsymbol{r} - \boldsymbol{r_1}| - 3i\pi/4)$, which coincides with the dominant term of the asymptotic expansion at $k|\boldsymbol{r} - \boldsymbol{r_1}| \to \infty$ of the exact solution $G(\boldsymbol{r}, \boldsymbol{r_1}) = -0.25i H_0^{(1)}(k|\boldsymbol{r} - \boldsymbol{r_1}|)$ of eq. (A3).

When ∇k has a constant direction and a normal mode propagates in this direction, that is, $(\boldsymbol{r} - \boldsymbol{r_1}) \cdot \nabla k \equiv 0$, horizontal rays (eq. A4) are again straight lines that connect points $\boldsymbol{r_1}$ and $\boldsymbol{r}$. In underwater acoustics, waveguides with this type of horizontal inhomogeneity are referred to as range-dependent ones. Choosing the Ox coordinate axis in the direction from $\boldsymbol{r_1}$ to $\boldsymbol{r}$, from eq. (A5) one finds

$$\Phi(\boldsymbol{r}, \boldsymbol{r}_1) = \int_{x_1}^{x} k dx. \tag{A6}$$

Note that geometry of the horizontal rays is independent of wave frequency in this case. Eq. (A6) for the mode phase is often applied to generic horizontally inhomogeneous waveguides and provides then an approximation to the true mode phase. In agreement with Fermat's principle, the difference between the true and approximate mode phase is of second order in the cross-range gradients of k, that is, in $\partial k/\partial y$. For a discussion of conditions of validity of the approximation (eq. A6) in generic horizontally inhomogeneous waveguides, see Godin (2002).

For the mode traveltime $t(\boldsymbol{r}, \boldsymbol{r_1})$ in a range-dependent waveguide, from eq. (A6) we find

$$t(\boldsymbol{r}, \boldsymbol{r}_1) = \frac{\partial \Phi(\boldsymbol{r}, \boldsymbol{r}_1)}{\partial \omega} = \int_{x_1}^{x} \frac{dx}{c_g} \tag{A7}$$

where $c_g = (\partial\omega/\partial k)_x$ is the group velocity of the mode in a corresponding horizontally homogeneous waveguide. Eq. (A7) has been used in the main text to calculate modal traveltimes and the modeled effective group speeds U shown in Fig. 4. Eq. (A7) shows that the effective group slowness, $U^{-1} = t(\boldsymbol{r}, \boldsymbol{r_1})/|\boldsymbol{r} - \boldsymbol{r_1}|$, in a range-dependent waveguide is an average of the modal slowness c_g^{-1} over range. When changes in k are due to changes in the ocean depth H and the depth varies steadily with range, the group slowness becomes a weighted average of c_g^{-1} over depth:

$$\frac{1}{U} = \frac{1}{H(x) - H(x_1)} \int_{H(x_1)}^{H(x)} \alpha \frac{dH}{c_g}, \quad \alpha = \frac{H(x) - H(x_1)}{(x - x_1) dH/dx}. \tag{A8}$$

As discussed in Appendix A, eq. (A8) helps to understand the striking difference in the frequency dependencies of U (see Fig. 4 in the main text) and c_g (see Fig. 3b in the main text).

APPENDIX B: DISPERSION EQUATION OF SCHOLTE WAVES IN A BENCHMARK PROBLEM

Consider a homogeneous water layer of depth H overlying a homogeneous solid half-space. The ratio of densities of the solid and the fluid is M. Wave frequency is ω; sound speed in water, and speeds of compressional and shear waves in the bottom are c, v_p and v_s, respectively.

The dispersion equation for such a waveguide is obtained by requiring that a monochromatic wave with a horizontal wavenumber k satisfies corresponding reduced wave equations in the fluid and the solid, conditions at infinity (i.e. only evanescent waves are allowed in the solid half-space), the boundary condition of zero acoustic pressure at the free upper surface of the water layer and the boundary condition at the fluid–solid interface. Three boundary conditions should be met at the fluid–solid interface: the normal (vertical) displacement is continuous, the normal (vertical) component of the traction vector is continuous and tangential (horizontal) components of the traction vector equal zero (Brekhovskikh & Godin 1998).

The resulting dispersion equation (Ewing *et al.* 1957) can be written as follows:

$$\frac{\tan\left(\omega H\sqrt{c^{-2}-v^{-2}}\right)}{\sqrt{c^{-2}-v^{-2}}} = \frac{M(v_s/v)^4}{\sqrt{v^{-2}-v_p^{-2}}}\left[4\sqrt{\left(1-\frac{v^2}{v_p^2}\right)\left(1-\frac{v^2}{v_s^2}\right)}-\left(2-\frac{v^2}{v_s^2}\right)^2\right]. \tag{B1}$$

Here, $v \equiv \omega/k$ is the phase speed of the normal mode. In all normal modes, $o \le v \le v_s$. Therefore, the right-hand side of eq. (B1) is always real. When $v < c$, it is convenient to write the left-hand side of eq. (B1) as $(v^{-2}-c^{-2})^{-1/2}\tanh(\omega H\sqrt{v^{-2}-c^{-2}})$. Note that the expression in the square brackets in the right-hand side of eq. (B1) is the same as appears in the dispersion equation for the Rayleigh surface wave in a solid half-space with a free boundary (Ewing *et al.* 1957; Brekhovskikh & Godin 1998). It is positive when $v < c_R$ and negative when v $> c_R$, where c_R is the Rayleigh surface wave speed in a solid half-space with a free boundary.

Every continuous, real-valued solution $v(\omega)$ of the dispersion eq. (B1) determines a dispersion curve of a particular normal mode. Surface waves supported by a fluid–solid interface and, more generally, normal modes in a fluid layer over a solid half-space are often referred to as Scholte–Stoneley or Scholte waves (Ewing *et al.* 1957; Brekhovskikh & Godin 1998).

In four special cases: (i) $M \to 0$, (ii) $M \to +\infty$, (iii) $H \to 0$ and (iv) $c_s \to 0$, the dispersion eq. (B1) reduces to well-known elementary dispersion equations (Ewing *et al.* 1957; Brekhovskikh & Godin 1998) for (i) a fluid layer with two free boundaries, (ii) a fluid layer with one free and one rigid boundary, (iii) Rayleigh surface wave in a solid half-space with a free boundary and (iv) the Pekeris waveguide, that is, a waveguide with a homogeneous fluid bottom. (In the case of a fluid bottom, there are no shear waves to carry energy to infinity, and the condition $0 \le v \le v_s$ no longer applies. It is replaced by $0 \le v \le v_p$.)

One can easily solve eq. (B1) explicitly for the product ωH as a function of v and parameters M, v_p, v_s and c:

$$\omega_0 H = \frac{1}{\sqrt{v^{-2}-c^{-2}}}\operatorname{arc\,tanh}\left(\frac{M(v_s/v)^4\sqrt{v^{-2}-c^{-2}}}{\sqrt{v^{-2}-v_p^{-2}}}\times\left[4\sqrt{\left(1-\frac{v^2}{v_p^2}\right)\left(1-\frac{v^2}{v_s^2}\right)}-\left(2-\frac{v^2}{v_s^2}\right)^2\right]\right), \quad 0 < v \le \min(c, c_R); \tag{B2}$$

$$\omega_0 H = \frac{1}{\sqrt{c^{-2}-v^{-2}}}\arctan\left(\frac{M(v_s/v)^4\sqrt{c^{-2}-v^{-2}}}{\sqrt{v^{-2}-v_p^{-2}}}\times\left[4\sqrt{\left(1-\frac{v^2}{v_p^2}\right)\left(1-\frac{v^2}{v_s^2}\right)}-\left(2-\frac{v^2}{v_s^2}\right)^2\right]\right), \quad c \le v \le c_R; \tag{B3}$$

$$\omega_n H = \frac{1}{\sqrt{c^{-2}-v^{-2}}}\left(\pi n-\arctan\left(\frac{M(v_s/v)^4\sqrt{c^{-2}-v^{-2}}}{\sqrt{v^{-2}-v_p^{-2}}}\times\left[\left(2-\frac{v^2}{v_s^2}\right)^2-4\sqrt{\left(1-\frac{v^2}{v_p^2}\right)\left(1-\frac{v^2}{v_s^2}\right)}\right]\right)\right), \quad c \le v \le v_s, \tag{B4}$$

where $n = 1, 2, \ldots$. Eqs (B2) and (B3) give the frequency of the fundamental mode with the phase speed v. The branch of its dispersion curve, which is described by eq. (B2), always exist; eq. (B3) describes an additional branch that exists provided $c < c_R$. The phase speed of the fundamental mode satisfies the inequality $v < c_R$.

Eq. (B4) gives the frequencies of the higher order modes with the phase speed v. Only the fundamental mode (eq. B2) exists when $c \ge v_s$. When $c < v_s$, the nth mode exists at frequencies $\omega \ge \Omega_n$ where the cut-off frequency

$$\Omega_n = \frac{1}{H\sqrt{c^{-2}-v_s^{-2}}}\left(\pi n-\arctan\left(\frac{M\sqrt{c^{-2}-v_s^{-2}}}{\sqrt{v_s^{-2}-v_p^{-2}}}\right)\right). \tag{B5}$$

Note that the cut-off frequency increases with decreasing ocean depth.

An explicit equation for the modal group speed

$$c_g = \frac{\partial\omega}{\partial k} = \left(1-\frac{\omega}{v}\frac{\partial v}{\partial\omega}\right)^{-1} v \tag{B6}$$

is readily obtained by differentiating both sides of eq. (B1) with respect to ω. The equation for c_g is cumbersome and will not be reproduced here. Fig. B1 shows group and phase dispersion curves modeled for the benchmark problem using the software of Herrmann & Ammon

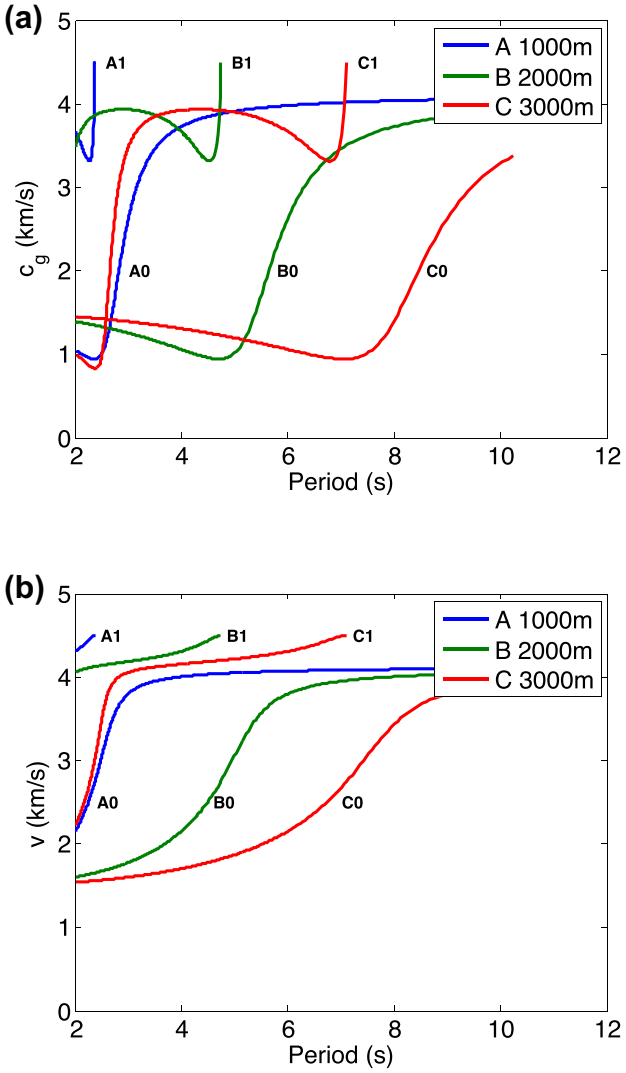

Figure B1. (a) Group dispersion curves for first two modes computed for the benchmark problem with water layer thicknesses of 1–3 km. Curves are labeled with the water depth of each model and the mode number (0 or 1). (b) Phase dispersion curves corresponding to the models shown in (a). Half-space compressional and shear velocities are 7.79 and 4.5 km s^{-1}, respectively, and the density ratio of the fluid layer to the half-space layer is $M = 3.0$.

(2004). We calculate dispersion for a model with density ratio $M = 3.0$, $c = 1.5\,\mathrm{km\,s^{-1}}$, $v_p = 7.79\,\mathrm{km\,s^{-1}}$ and $v_s = 4.5\,\mathrm{km\,s^{-1}}$. Dependencies of the modal phase and group velocities on wave period $2\pi/\omega$ in the benchmark problem, which follow from eq. (B1), are qualitatively similar to those shown in Figs 3b and c in the main text.

It follows from eqs (B1) and (B6) that the modal phase and group velocities are functions of the product ωH when the parameters M, c, v_p and v_s are kept constant. (v and c_g retain this property also in other waveguides as long as the acoustic impedance (Brekhovskikh & Godin 1998) of the boundary $z = H$ is a function of v and is independent of frequency.) For any function of ωH, averaging over frequency is equivalent to averaging over ocean depth. Indeed, the average over frequency

$$\frac{1}{\omega_2 - \omega_1}\int_{\omega_1}^{\omega_2} f(\omega H)d\omega = \frac{1}{\omega_2 H - \omega_1 H}\int_{\omega_1 H}^{\omega_2 H} f(a)da \tag{B7}$$

equals the average over depth

$$\frac{1}{H_2 - H_1}\int_{H_1}^{H_2} f(\omega H)dH = \frac{1}{\omega H_2 - \omega H_1}\int_{\omega H_1}^{\omega H_2} f(a)da \tag{B8}$$

as long as $\omega_1 H = \omega H_1$ and $\omega_2 H = \omega H_2$.

As discussed in Appendix A, mode traveltime in a waveguide with range-dependent bathymetry is proportional to an average of c_g^{-1} over ocean depth H. In the benchmark problem we consider, averaging over H at fixed ω is equivalent to averaging over ω at fixed H and results in a suppression of the frequency dependence of the modal traveltime.